LETTERS

Shallow fault-zone dilatancy recovery after the 2003 Bam earthquake in Iran

Eric J. Fielding[1], Paul R. Lundgren[1], Roland Bürgmann[2] & Gareth J. Funning[3]

Earthquakes radiate from slip on discrete faults, but also commonly involve distributed deformation within a broader fault zone, especially near the surface. Variations in rock strain during an earthquake are caused by heterogeneity in the elastic stress before the earthquake, by variable material properties and geometry of the fault zones, and by dynamic processes during the rupture[1,2]. Stress changes due to the earthquake slip, both dynamic and static, have long been thought to cause dilatancy in the fault zone that recovers after the earthquake[3–5]. Decreases in the velocity of seismic waves passing through the fault zone due to coseismic dilatancy have been observed[6] followed by postseismic seismic velocity increases during healing[5,7,8]. Dilatancy and its recovery have not previously been observed geodetically. Here we use interferometric analysis of synthetic aperture radar images to measure postseismic surface deformation after the 2003 Bam, Iran, earthquake and show reversal of coseismic dilatancy in the shallow fault zone that causes subsidence of the surface. This compaction of the fault zone is directly above the patch of greatest coseismic slip at depth. The dilatancy and compaction probably reflects distributed shear and damage to the material during the earthquake that heals afterwards. Coseismic and postseismic deformation spread through a fault zone volume may resolve the paradox of shallow slip deficits for some strike-slip fault ruptures[9].

Several seismic studies have found that the ratio of the velocities of S waves to P waves decreases with time after an earthquake, in addition to an overall velocity increase, reflecting a postseismic increase in the Poisson's ratio of fault zone material; this increase in Poisson's ratio is interpreted as an increase in the fraction of pore space filled with liquid[6,7] as the fault zone contracts. These postseismic changes reverse the coseismic velocity changes due to dilatancy in the fault zone. Seismic waves are relatively insensitive to the depth of the anomalies, but the damaged fault zone may be confined to the top 3–4 km of the crust and possibly to very shallow (~200 m) depths[8].

Fault zone dilatancy is caused by pervasive damage where small cracks open up within the deformed rocks, increasing the porosity and volume[3–5]. It has been difficult to measure the predicted coseismic dilatancy and postseismic volume decrease in earthquake fault zones geodetically, because dilatancy occurs within a very narrow damage zone along the earthquake rupture and many other postseismic processes also cause deformation of the Earth's surface.

Geodetic measurements of far-reaching postseismic deformation for many large earthquakes have been modelled as a combination of viscous relaxation in the lower crust and upper mantle and with aseismic afterslip on a deep continuation of the fault that ruptured[10]. Postseismic deformation in the upper crust has been explained by pore-pressure transients[11,12] and by afterslip both immediately surrounding coseismic slip patches and up-dip from the coseismic rupture[13–15], which can overwhelm the deformation from dilatancy recovery. We exploit interferometric synthetic aperture radar (InSAR) to measure negative volume change in the fault zone after a large earthquake in Iran.

Here we analyse 3.5 years of postseismic deformation after the M_w (moment magnitude) 6.6 earthquake that devastated the city of Bam, Iran, on 26 December 2003, using synthetic aperture radar from the European Space Agency Envisat satellite. The earthquake primarily ruptured a buried strike-slip fault that extends under the city of Bam and beneath a broad alluvial plain to the south[16–21]. This fault is part of a broad system of north–south oriented, right-lateral shear in eastern Iran[19]. Because the first synthetic aperture radar image was acquired 12 days after the earthquake, we cannot separate the earliest phase of postseismic deformation from the coseismic deformation. The stable surface around Bam provides optimal InSAR coherence[18] for mapping deformation during and after the earthquake. The surface rupture from coherence and field mapping[16,18] propagated from the south towards Bam[19]. Inversion of the surface deformation measured by InSAR[9,17], cross-correlation of optical imagery, and levelling data[20,21] require slip >2 m at depths of 4–5 km on the main fault, with less near the surface and little slip north of Bam. Maximum offsets across the surface ruptures were 0.25 m (refs 16, 18, 19), but total shear across a zone about 1 km wide is >1 m (refs 17, 21). A less pronounced shallow slip deficit has also been found for some other large strike-slip earthquakes[9]. We concentrate on surface displacement features with spatial scales less than 10 km that can resolve deformation in roughly the upper 8 km of the crust, because atmospheric effects mask InSAR signals at larger scales[22].

Two features stand out in the postseismic deformation, with different spatial scales and temporal behaviour. We examine the hypotheses that these are caused by (1) afterslip, (2) localized poroelastic rebound at a restraining bend of the coseismic rupture, and (3) localized compaction of material that dilated during the earthquake. The first major feature in the postseismic pattern is two lobes of line-of-sight (LOS) change near the south end of the main coseismic rupture with positive LOS motion (towards the satellite locations) to the east of the rupture (A1 and A2 on Fig. 1 and Supplementary Fig. 5) and alternating zones of positive and negative LOS motion that have much lower amplitude, but similar spatial extent, about 10 km further north. The descending track (no. 120) is dominated by strong positive LOS motion (towards the satellite locations) to the southeast of the rupture (A1), whereas the ascending tracks (nos 156 and 385) have a smaller area of positive amplitude to the east combined with negative LOS motion to the west (A2), requiring a substantial eastward component of displacement. The combination of these features is consistent with afterslip above and to the south of the main coseismic asperity that ruptured during the 2003 earthquake. The time series shows that the afterslip rate decayed with a time constant of ~335 days if an exponential time function is assumed (Fig. 2a).

[1]Jet Propulsion Laboratory, California Institute of Technology, 4800 Oak Grove Drive, Pasadena, California 91109, USA. [2]Department of Earth and Planetary Science, University of California, Berkeley, California 94720, USA. [3]Department of Earth Science, University of California, Riverside, California 92521, USA.

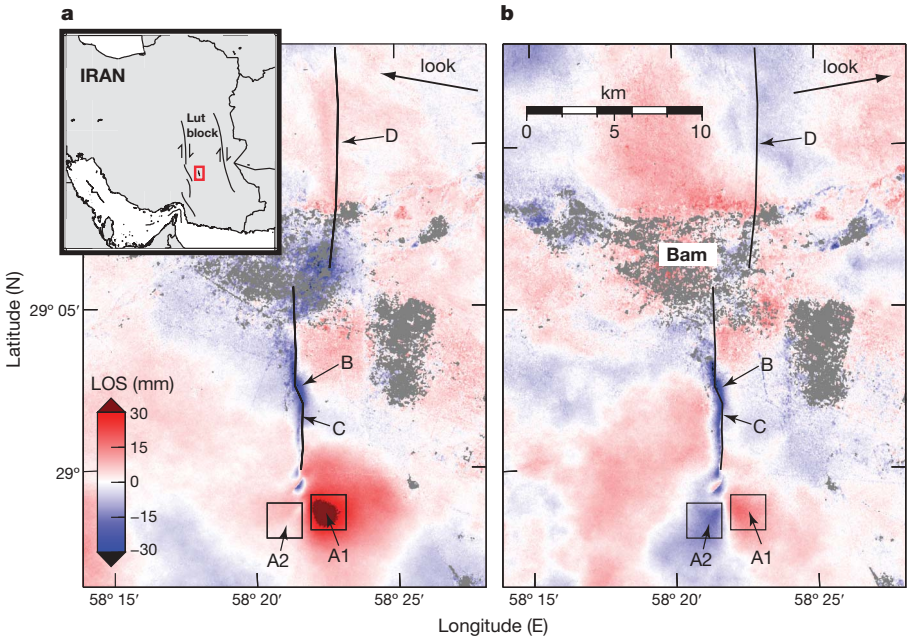

Figure 1 | Postseismic surface deformation after the Bam, Iran, earthquake. **a**, **b**, Maps from two Envisat tracks in radar lines-of-sight (LOS); fits to each time series have been converted to estimates of total displacement between 12 and 1,097 days after the 26 December 2003 earthquake. Black lines, locations of coseismic fault ruptures mapped from InSAR[18]. Difference of boxes A1 and A2, used for Fig. 2a, measures afterslip at 2–3 km depth. Subsidence at B is poroelastic and at C is recovery of dilatancy. D is minor uplift on northern fault. **a**, Descending track no. 120. **b**, Ascending track no. 156. Horizontal components of look vectors shown with arrows. Inset, location of Bam in southeast Iran.

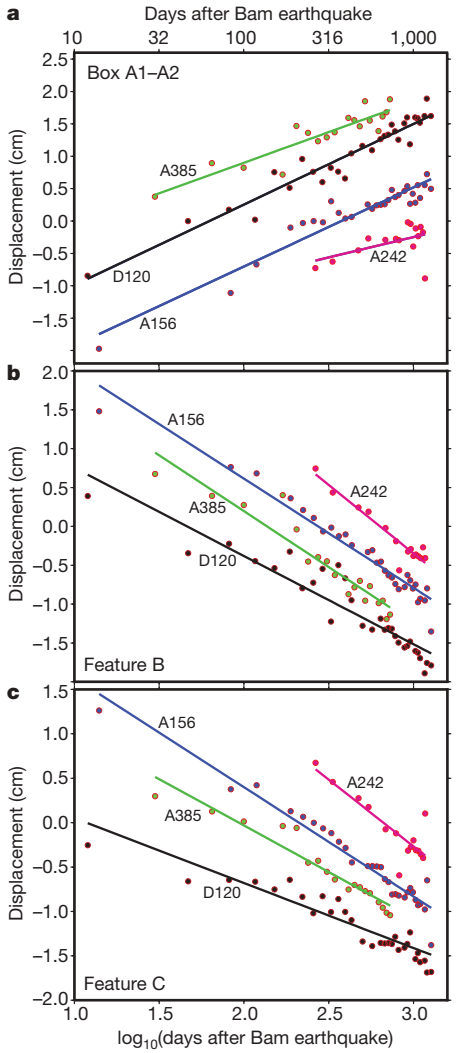

Second, the spatial pattern (see Fig. 1) includes a narrow zone of >20 mm subsidence combined with horizontal motion towards the coseismic surface ruptures observed south of the city of Bam[16,18]. Subsidence is strongest near a left bend of the right-lateral fault (feature B in Fig. 1) and continues along a roughly 500-m-wide zone north and south of the bend (feature C). This zone continued to subside for at least 3.5 years after the earthquake (Fig. 2b, c). We advocate that this subsidence has both poroelastic (feature B) and dilatancy recovery (feature C) components.

Readjustment of pore fluid pressure (poroelastic rebound) in the crust can cause volume changes following earthquakes, resulting in postseismic subsidence over areas of coseismic pressure increase and vice versa. The widest and strongest subsidence south of Bam is where the left bend caused compression (feature B on Figs 1 and 3) and coseismic uplift of at least 60 mm (Supplementary Fig. 6). A large part of the postseismic subsidence there is probably due to a poroelastic response reflecting partial deflation of the coseismic uplift due to fluid flow away from the compressed fault bend. Early relaxation in the first 12 days after the earthquake is included in the coseismic interferogram and cannot be measured. The Bam fault-bend subsidence has a nearly log-linear rate out to the end of the 3.5 years we analysed; the relaxation time for an exponential decay fit is 1.7 years.

The postseismic subsidence along the rupture zone south of Bam, however, extends >2 km to the north and >4 km south of the left bend in the fault (C in Fig. 3); this requires another process in addition to poroelastic rebound in the restraining bend, as the rest of the zone experienced no measurable coseismic compression. To the south of the bend, the surface ruptures mapped in the field[16,18]

Figure 2 | Postseismic deformation of features as function of time. **a**, Time series of difference between range change of boxes A1 and A2 (see Fig. 1) plotted versus the logarithm of the time in days since the earthquake, for four Envisat tracks. Lines show least squares fits with the log(t) function; line colour is keyed to data. Prefixes A and D denote respectively ascending and descending tracks. **b**, Subsidence in fault bend due to poroelastic rebound from difference between polygon B and boxes to east and west (see Fig. 3). **c**, Subsidence south of fault bend (difference between polygon C and two adjacent boxes, see Fig. 3) interpreted as recovery of coseismic dilatancy in the shallow fault zone.

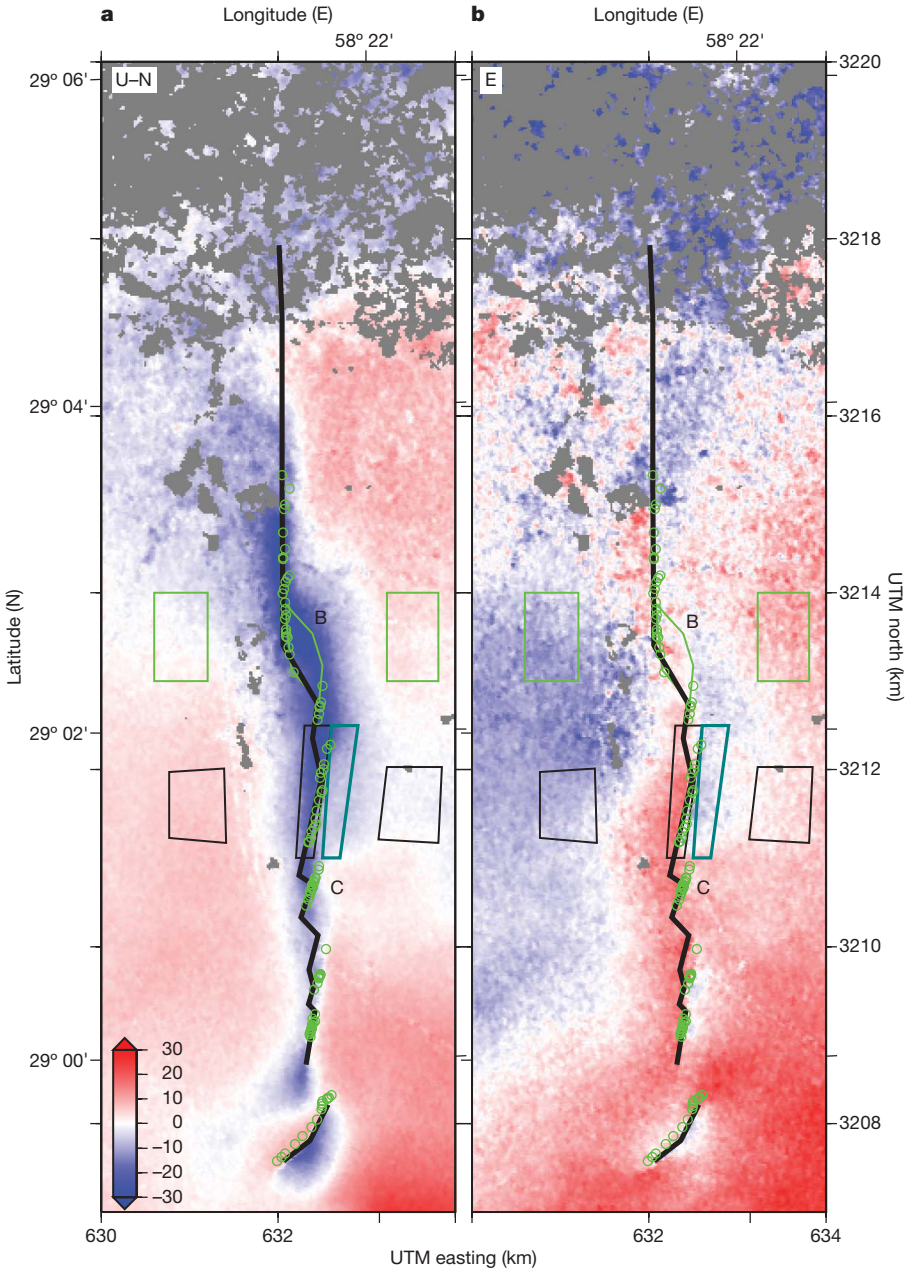

Figure 3 | Transformed components of total displacement from tracks 120 and 156. **a**, **b**, Components in mm (colour scale) for the area of the main coseismic rupture south of Bam, showing the narrow zone of subsidence along the fault: **a**, 'up' minus 0.1×'north' (U − N); **b**, 'east' (E). Black lines, locations of coseismic rupture from InSAR; green circles, locations of coseismic rupture mapped in the field[18]. Boxes B and C used for time series plots of Fig. 2b and c, respectively. On left, labelled and unlabelled tickmarks show respectively latitude and UTM (universal transverse Mercator projection, zone 40) north; and vice versa for tickmarks on right.

included a small opening component, indicating east–west coseismic expansion in the surface layer, which is also reflected in the coseismic InSAR[17,18]. The postseismic InSAR shows that there is a net motion of the surface on both sides of the fault towards the fault south of the bend (see Fig. 3b), which suggests that there was coseismic dilation or damage in the fault zone that subsequently relaxed. The material that compacted after the earthquake apparently did not have enough fluid flowing inward to fill the dilated pore space created during the earthquake to counteract the compaction and subsidence. There is no indication of dilatancy recovery along the rupture segment north of Bam (feature D in Fig. 1), where a small amount of postseismic uplift indicates different material properties or stress conditions of the shallow fault zone.

To explore the processes and kinematics of the postseismic transients that cause the surface deformation features, we utilize elastic half-space dislocation models. We model the afterslip using the two planar faults of the coseismic model: a near-vertical right-lateral strike-slip fault and an oblique-slip (fixed rake 151°) thrust dipping 64° to the west[17]. The preferred afterslip distribution on these faults has 100–136 mm of afterslip above and to the south of the large coseismic slip area on the main fault, and also has afterslip on the secondary fault just below the afterslip on the main fault (Supplementary Fig. 7). The peak afterslip is at about 3 km depth in the south and shallower than 2 km depth to the north. We explored alternative fault geometries, but few aftershocks were located in the area south of the main coseismic rupture to provide constraints on the fault geometry[23]. None of the afterslip models explain the narrow zone of subsidence along the main fault.

Broad-scale surface rebound due to pore-pressure relaxation after the coseismic stress change can be approximated by taking the difference

between surface deformation fields of undrained and drained elastic models[24]. The predicted deformation is opposite in sign from coseismic displacements and from postseismic deformation (see Fig. 1 and Supplementary Fig. 9). We cannot rule out a small amount (<10 mm) of broad-scale poroelastic rebound in the first two months after the Bam earthquake because longer-wavelength atmospheric effects are particularly strong in the two Envisat scenes acquired in early January 2004, obscuring deformation at scales greater than about 5 km.

We model the compaction of the fault zone with a grid of regularly spaced contracting Mogi point sources in an elastic half-space. This simple approximation allows efficient computations, but does not directly model the physical process that must involve a more continuous contracting volume. We performed an inversion with both the contracting Mogi source array and afterslip on the main rupture to determine an optimum joint distribution of deformation sources. The afterslip in the joint model is similar to the two-fault afterslip model, and the contraction sources are concentrated in a band that is deeper and stronger in the northern part (see Fig. 4c). The vertical extent of the contraction band depends on the amount of smoothing applied in the inversion, but the depth is constrained by the width of the observed subsidence. This model fits the measured subsidence and horizontal contraction (Figs 3 and 4). Our data only resolve contraction in the upper kilometre of the fault zone (with a total volume decrease of 8.4×10^4 m^3); however, 2×10^5 m^3 of dilatancy recovery could have occurred on the remaining coseismic slip zone below 1 km depth without producing significant surface deformation. Because the magnitude of coseismic dilatancy and its recovery is likely to be reduced at greater depths and confining pressures[25], dilatancy processes may have occurred at greater depths but are not resolved by geodetic data.

The restricted spatial extent and the three years of increasing subsidence in the fault zone south of Bam is very different from the broad-scale elevation changes of 1–2 months duration interpreted as pore-pressure transients after a similar earthquake in Iceland[11]. The Bam poroelastic response has a much longer time constant (Fig. 2b) than the relaxation time of 0.75 years estimated for Landers[24] and about 2 months for the Iceland earthquake[11]. The >1.7 year relaxation time for the Bam fault-bend subsidence (feature B) implies that the poroelastic rock volume has lower permeability.

The zone of strong postseismic contraction in the fault zone (Fig. 4) is directly above the largest coseismic slip[9,17], where the coseismic surface ruptures were widest and had the largest offsets in InSAR and field mapping[18]. This is also where coseismic optical and synthetic aperture radar pixel offsets show ~1 m of right-lateral shear over about 1 km centred on the fault[17,21]. It is impossible to determine from the surface displacements alone what part of the shear is elastic versus inelastic deformation, but theoretical models of deformation of porous media predict that shear at shallow depths is likely to involve damage with a dilatancy component[25]. The postseismic contraction occurred in the area where coseismic fault zone shear and hence damage were strongest. The depth of the contraction probably reflects the distribution of coseismic dilatancy; this is controlled by material strength variations and by distribution of water in the shallow crust, both modulated by stress.

We conclude that the localized postseismic subsidence over the Bam fault zone is partly due to a combination of afterslip above and to the south of the high-slip zone of the earthquake, together with poroelastic rebound in a prominent restraining bend in the rupture: this subsidence is dominated by healing and compaction of coseismic dilatation and damage in the upper ~1 km of the fault zone outside of the bend[25]. The postseismic compaction at Bam is approximately logarithmic in time, consistent with measurements of changes in the velocities of seismic waves in fault zones[5–8].

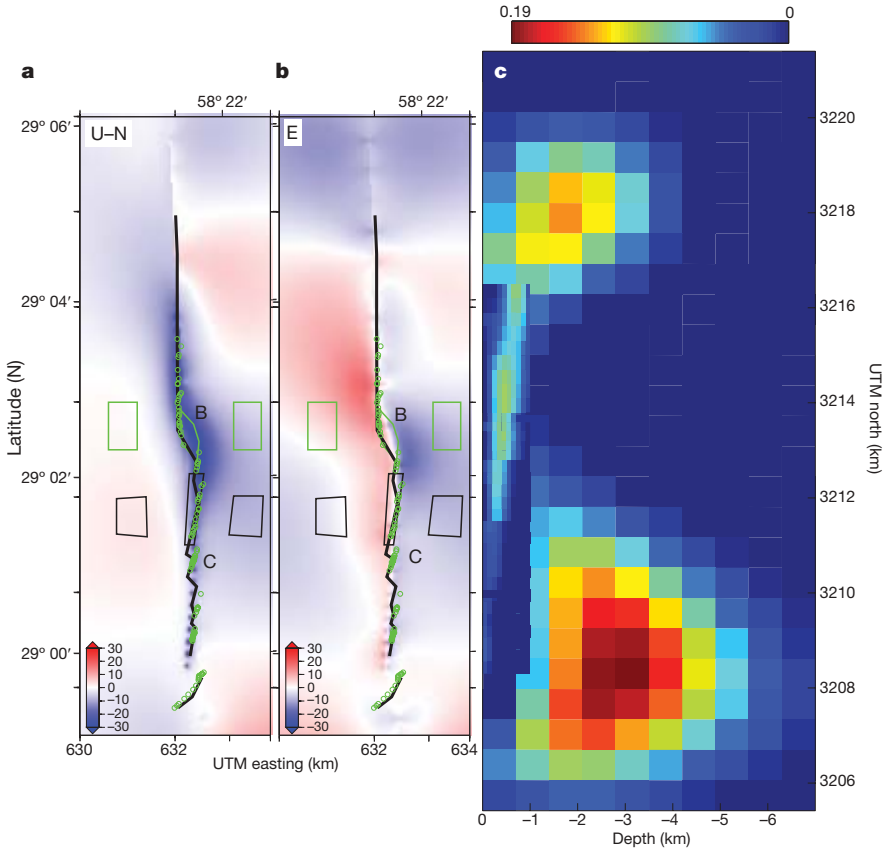

Figure 4 | Shallow fault zone contraction and main fault afterslip combined model results. Maps of predicted deformation in mm (colour scale) for the same area as Fig. 3; **a**, 'up' minus 0.1×'north' (U–N), and **b**, 'east' (E). **c**, Model source strength shown in north–south profile aligned with maps. Depth in km on horizontal axis. Shallow fault zone volume decrease (in 10^4 m^3) is shown as colour of small rectangles; main fault afterslip magnitude (in m) is shown as colour of large squares (same colour scale). Some afterslip patches are hidden behind the shallow fault zone.

METHODS SUMMARY

We formed 342 full-resolution interferograms from 94 Envisat ASAR (advanced synthetic aperture radar) scenes on four different satellite tracks acquired between 7 January 2004 and 22 June 2007 (Supplementary Tables 1–4 and Supplementary Figs 1–4) using the JPL/Caltech ROI_pac[26] and Stanford SNAPHU[27] software. We calculated time series of line-of-sight (LOS) deformation for each track using a modified small baseline subset algorithm[28] (see Supplementary Information for full Methods description). The LOS vectors for the four tracks are nearly coplanar, so the north component of ground motion is poorly constrained (Supplementary Table 5). The temporal resolution is determined by the 35-day repeat cycle of the Envisat orbit and the spatial resolution is approximately 20×20 m on the ground.

We mitigate atmospheric errors by computing the total LOS-change maps from a number of independent measurements. Long-wavelength errors due to atmospheric effects and imprecise orbit knowledge were reduced by fitting and removing a planar phase gradient from a 40×40 km subset of each date's solution (Fig. 1, Supplementary Fig. 5). This also removes any long-wavelength deformation signal, so we cannot resolve postseismic deformation due to viscoelastic relaxation or afterslip in the lower crust or mantle.

For efficient model parameter optimization, we selected about 1,000 samples from estimated total deformation for the target area (Fig. 1, Supplementary Fig. 5) from each of the four tracks using a source-dependent sampling method[29] with the main coseismic rupture planes[17] as the sources. Green's functions relating dislocations (shear or tensile) on fault patches to deformation at the surface were calculated with the Poly3D program[30]. We optimized the distribution of dislocation magnitudes on fixed-geometry surfaces with a non-negative least squares procedure including a smoothing constraint. In the joint source modelling, we used a shallow fault extending to 2 km depth along the main coseismic rupture to optimize the sampling. Details are in Supplementary Information.

Received 6 July 2008; accepted 9 January 2009.

1. Mai, P. M. & Beroza, G. C. A spatial random field model to characterize complexity in earthquake slip. *J. Geophys. Res.* **107,** 2308, doi:10.1029/2001JB000588 (2002).
2. Ben-Zion, Y. & Sammis, C. G. Characterization of fault zones. *Pure Appl. Geophys.* **160,** 677–715 (2003).
3. Nur, A. Effects of stress on velocity anisotropy in rocks with cracks. *J. Geophys. Res.* **76,** 2022–2034 (1971).
4. Scholz, C. H. Post-earthquake dilatancy recovery. *Geology* **2,** 551–554 (1974).
5. Vidale, J. E. & Li, Y.-G. Damage to the shallow Landers fault from the nearby Hector Mine earthquake. *Nature* **421,** 524–526 (2003).
6. Li, Y.-G., Chen, P., Cochran, E. S., Vidale, J. E. & Burdette, T. Seismic evidence for rock damage and healing on the San Andreas Fault associated with the 2004 M 6.0 Parkfield earthquake. *Bull. Seismol. Soc. Am.* **96,** S349–S363 (2006).
7. Schaff, D. P. & Beroza, G. C. Coseismic and postseismic velocity changes measured by repeating earthquakes. *J. Geophys. Res.* **109,** B10302, doi:10.1029/2004JB003011 (2004).
8. Peng, Z. G. & Ben-Zion, Y. Temporal changes of shallow seismic velocity around the Karadere-Düzce branch of the North Anatolian Fault and strong ground motion. *Pure Appl. Geophys.* **163,** 567–600 (2006).
9. Fialko, Y., Sandwell, D., Simons, M. & Rosen, P. A. Three-dimensional deformation caused by the Bam, Iran, earthquake and the origin of shallow slip deficit. *Nature* **435,** 295–299 (2005).
10. Bürgmann, R. & Dresen, G. Rheology of the lower crust and upper mantle: Evidence from rock mechanics, geodesy and field observations. *Annu. Rev. Earth Planet. Sci.* **36,** 531–567 (2008).
11. Jónsson, S., Segall, P., Pedersen, R. & Bjornsson, G. Post-earthquake ground movements correlated to pore-pressure transients. *Nature* **424,** 179–183 (2003).
12. Peltzer, G., Rosen, P., Rogez, F. & Hudnut, K. Postseismic rebound in fault step-overs caused by pore fluid-flow. *Science* **273,** 1202–1204 (1996).
13. Johanson, I. A., Fielding, E. J., Rolandone, F. & Burgmann, R. Coseismic and postseismic slip of the 2004 Parkfield earthquake from geodetic data. *Bull. Seismol. Soc. Am.* **96,** S269–S282 (2006).
14. Langbein, J., Murray, J. R. & Snyder, H. A. Coseismic and initial postseismic deformation from the 2004 Parkfield, California, earthquake, observed by global positioning system, electronic distance meter, creepmeters, and borehole strainmeters. *Bull. Seismol. Soc. Am.* **96,** S304–S320 (2006).
15. Hsu, Y. J. *et al.* Frictional afterslip following the 2005 Nias-Simeulue earthquake, Sumatra. *Science* **312,** 1921–1926 (2006).
16. Talebian, M. *et al.* The 2003 Bam (Iran) earthquake: Rupture of a blind fault. *Geophys. Res. Lett.* **31,** L11611, doi:10.1029/2004GL020058 (2004).
17. Funning, G. J., Parsons, B. E., Wright, T. J., Jackson, J. A. & Fielding, E. J. Surface displacements and source parameters of the 2003 Bam (Iran) earthquake from Envisat advanced synthetic aperture radar imagery. *J. Geophys. Res.* **110,** B09406, doi:10.1029/2004JB003338 (2005).
18. Fielding, E. J. *et al.* Surface ruptures and building damage of the 2003 Bam, Iran, earthquake mapped by satellite synthetic aperture radar interferometric correlation. *J. Geophys. Res.* **110,** B03302, doi:10.1029/2004JB003299 (2005).
19. Jackson, J. A. *et al.* Seismotectonic, rupture-process, and earthquake-hazard aspects of the 26 December 2003 Bam, Iran, earthquake. *Geophys. J. Int.* **166,** 1270–1292 (2006).
20. Motagh, M. *et al.* Combination of precise leveling and InSAR data to constrain source parameters of the Mw= 6.5, 26 December 2003 Bam earthquake. *Pure Appl. Geophys.* **163,** 1–18 (2006).
21. Peyret, M. *et al.* The source motion of 2003 Bam (Iran) earthquake constrained by satellite and ground-based geodetic data. *Geophys. J. Int.* **169,** 849–865 (2007).
22. Bürgmann, R., Rosen, P. A. & Fielding, E. J. Synthetic aperture radar interferometry to measure Earth's surface topography and its deformation. *Annu. Rev. Earth Planet. Sci.* **28,** 169–209 (2000).
23. Sadeghi, H., Aghda, S. M. F., Suzuki, S. & Nakamura, T. 3-D velocity structure of the 2003 Bam earthquake area (SE Iran): Existence of a low-Poisson's ratio layer and its relation to heavy damage. *Tectonophysics* **417,** 269–283 (2006).
24. Peltzer, G., Rosen, P., Rogez, F. & Hudnut, K. Poroelastic rebound along the Landers 1992 earthquake surface rupture. *J. Geophys. Res.* **103,** 30131–30145 (1998).
25. Hamiel, Y., Lyakhovsky, V. & Agnon, A. Coupled evolution of damage and porosity in poroelastic media: Theory and applications to deformation of porous rocks. *Geophys. J. Int.* **156,** 701–713 (2004).
26. Rosen, P. A., Hensley, S., Peltzer, G. & Simons, M. Updated repeat orbit interferometry package released. *Eos* **85,** 47 (2004).
27. Chen, C. W. & Zebker, H. A. Network approaches to two-dimensional phase unwrapping: Intractability and two new algorithms. *J. Opt. Soc. Am. A* **17,** 401–414 (2000).
28. Berardino, P., Fornaro, G., Lanari, R. & Sansosti, E. A new algorithm for surface deformation monitoring based on small baseline differential SAR interferograms. *IEEE Trans. Geosci. Rem. Sens.* **40,** 2375–2383 (2002).
29. Lohman, R. B. & Simons, M. Some thoughts on the use of InSAR data to constrain models of surface deformation: Noise structure and data downsampling. *Geochem. Geophys. Geosyst.* **6,** Q01007, doi:10.1029/2004GC000841 (2005).
30. Thomas, A. L. *Poly3D: A Three-Dimensional, Polygonal Element, Displacement Discontinuity Boundary Element Computer Program with Applications to Fractures, Faults, and Cavities in the Earth's Crust*. M.Sc. Thesis, Stanford Univ. (1993).

Supplementary Information is linked to the online version of the paper at www.nature.com/nature.

Acknowledgements Envisat data are copyright 2004–07 European Space Agency and were provided under AOE project 668. We thank R. Lohman for the use of data resampling programs and discussions. We thank J. Jackson, M. Talebian, D. McKenzie, J.-P. Avouac, Z. Liu, Z.H. Li, E. Cochran, F. Horowitz, G. Peltzer, Y. Ben-Zion and E. Hearn for discussions. Part of this research was performed at the Jet Propulsion Laboratory, California Institute of Technology, under contract with the National Aeronautics and Space Administration.

Author Contributions E.J.F. performed the data analysis, interpretation and modelling. P.R.L. wrote the time series analysis and modelling framework programs, and contributed to interpretation. R.B. and G.J.F. contributed to modelling and interpretation. E.J.F. and R.B. wrote the manuscript with contributions from all authors.

Author Information Reprints and permissions information is available at www.nature.com/reprints. Correspondence and requests for materials should be addressed to E.J.F. (Eric.J.Fielding@jpl.nasa.gov).

Author Queries

Journal: **Nature**
Paper: **nature07817**
Title: **Shallow fault-zone dilatancy recovery after the 2003 Bam earthquake in Iran**

Query Reference	Query
1	AUTHOR: When you receive the PDF proofs, please check that the display items are as follows (doi:10.1038/nature07817): Figs 1, 2, 3, 4 (colour); Tables: None; Boxes: None. Please check all figures (and tables, if any) very carefully as they have been re-labelled, re-sized and adjusted to Nature's style.
2	AUTHOR: Thank you for clarifying continuing subsidence; I have added 'for' for clarity; please check wording

For Nature office use only:

Layout	☐	Figures/Tables/Boxes	☐	References	☐
DOI	☐	Error bars	☐	Supp info (if applicable)	☐
Title	☐	Colour	☐	Acknowledgements	☐
Authors	☐	Text	☐	Author contribs (if applicable)	☐
Addresses	☐	Methods (if applicable)	☐	COI	☐
First para	☐	Received/Accepted	☐	Correspondence	☐
Display items	☐	AOP (if applicable)	☐	Author corrx	☐

Notes on InSAR data and processing

Envisat ASAR (advanced synthetic aperture radar) scenes for each track (descending track 120 and ascending tracks 156, 385 and 242) were sorted by their perpendicular baseline (see tables S1-S4) to determine which pairs had perpendicular baselines less than a threshold. The perpendicular baseline determines how sensitive the InSAR pair is to the topography, so a smaller baseline is better for measuring deformation. The area around Bam has very little relief, so we use longer baselines than in other studies to improve the time series (see following section). For tracks D120 and A156, the maximum perpendicular baseline was 300 m; the number of pairs was 106 and 109, respectively (see Figs. S1 and S2). For track A242, we used pairs up to 450 m baseline and for track 385 we used pairs up to 600 m baseline, because those tracks had fewer scenes acquired; the number of pairs was 60 and 67, respectively (see Figs. S3 and S4). The Doris precision (VOR) orbits from ESA were used for all orbit calculations.

All interferogram pairs (Figs. S1-S4) were processed with the JPL/Caltech ROI_pac software (Rosen et al., 2004), with no averaging in the cross-track (range) direction and averaging 5 pixels in the along-track (azimuth) direction to give an interferogram pixel size about 20 by 20 m on the ground. Data was processed from the raw (level 0) products. We used a one-arcsecond spacing digital elevation model (DEM) from the Shuttle Radar Topography Mission (SRTM), version 1, projected into UTM (universal transverse Mercator) zone 40 coordinates at 20 m spacing in the processing. A low-pass filter using a 3 by 3 pixel boxcar smoothing window was applied to the data

before unwrapping with the Stanford SNAPHU program (Chen and Zebker, 2002). The SNAPHU program unwraps the phase of all the pixels of the interferogram but the results are not reliable in low coherence areas, mostly in the vegetated agricultural areas of Bam and the adjacent town of Baravat (Fielding et al., 2005). The interferograms were masked to remove pixels with correlation smaller than 0.4 after the unwrapping step. The output geocoding was done at 20 m spacing in UTM coordinates for an area of 38 by 41 km (1916 by 2051 pixels) surrounding the city of Bam.

Notes on Time series analysis

We performed time series analysis with the small-baseline subset (SBAS) algorithm (Berardino et al., 2002) on the geocoded full-resolution interferograms for each of the four tracks. The SBAS technique involves solving a matrix equation for each pixel in the stack of interferograms:

$$\mathbf{Bv} = \delta\boldsymbol{\phi} \qquad \text{(S1)}$$

that relates the phase or range change ($\delta\boldsymbol{\phi}$) of the pixel relative to a reference image (marked with a "*" in tables S1-S4) on each observation date to the range change of the interferogram pairs through the velocity **v** or rate of range change vs. time through the matrix **B** that contains the time intervals of each interferogram on the diagonal (Berardino et al., 2002). The equation is solved using singular value decomposition. The reference image for each track was chosen to minimize the atmospheric effects on the time series, because atmospheric delay variations in the reference image will be mapped into all of the other dates. By using the range change velocity instead of the displacement in equation S1, disconnected subsets, such as the two scenes at the bottom of Fig. S2, can be combined with the other interferograms to estimate the range change of those dates

relative to the reference (Berardino et al., 2002). No spatial or temporal smoothing was applied to the time series results in order to keep the highest possible spatial and temporal resolution, but a best fitting plane was removed from the solution for each date in the time series.

The SBAS analysis that we used does not assume a specific functional form for the deformation in space or time. Postseismic deformation has been modeled with a number of different functions of time to match the typical decreasing rate of deformation after the earthquake. The simplest function of time that has been used to fit postseismic deformation u is:

$$u = a + b\log(t) \qquad \text{(S2)}$$

where t is the time since the earthquake and a and b are constants (Savage et al., 2005). This time function has the disadvantage of going to negative infinity at time t=0, the time of the earthquake. It has the advantage of only two adjustable parameters and the first InSAR data was acquired 12 days after the Bam earthquake so we are far from time t=0. By substituting t'=log(t), it is trivial to solve for parameters a and b with standard linear regression. We used this means to solve for the log-slope parameter b or log-linear velocity that best fits the time series for each pixel in the time series for each track. To reduce the effects of errors in the SRTM topographic data with the long baselines included in our InSAR analysis, we modified the method described in (Berardino et al., 2002) that solved for a linear velocity and topographic error at each pixel by least-squares match to the set of interferograms (and their associated baselines) for each track; we solved for the log-linear velocity and topographic error terms for each pixel. The time series for the four tracks cover different time intervals after the Bam earthquake (see

Tables S1-S4), so we used the same 4.5 ln(*years*) or 1.95 $\log_{10}$(*days*) time interval to convert the log-linear velocities to an estimate of the total deformation from 12 days to 1097 days after the earthquake. This is the estimated total deformation shown in Figs. 1, 3 and S5.

Notes on Displacement components

As mentioned in the main text, the four Envisat InSAR scenes have LOS vectors that are nearly coplanar (see Table S5). This means that it is not possible to accurately estimate all three orthogonal components of the surface displacements. In particular, the InSAR range-change measurements have low sensitivity to the north component of surface displacements. We can separate the east component of displacements from a second component that is a mixture of up and north, which we show in Figs. 3 and 4. The area of interest near Bam is close to the center of ascending track 156 and descending track 120 which have the same beam mode, so the LOS vectors are symmetric about the north-south plane (see Table S5). Assuming a constant line-of-sight for the 38 by 41 km area of the analysis, we calculate the *east* component as $1.3(r_{120} - r_{156})$ where r_{120} is the range change of track D120 and r_{156} is that of track A156 (Fielding et al., 2005). This *east* component is shown in Figs. 3b and 4b. The other component is *up* minus 10% of *north* displacement, which we calculate as $0.54(r_{120} + r_{156})$, shown in Figures 3a and 4a (Fielding et al., 2005). We use only tracks 120 and 156 to calculate the postseismic components because those have the longest time series and therefore the lowest level of atmospheric noise in the estimated total postseismic deformation shown in Figs. 1 and 3.

A similar *up* minus *north* component was calculated for the coseismic deformation using the coseismic interferograms from tracks D120 and A385 (Fielding et

al., 2005) (no prequake scene was acquired on track A156, so there is no coseismic interferograms for that track). This component is shown in Fig. S6 with the same area and overlays as Fig. 3. Note the strong localized uplift in the fault left bend marked B, caused by the compressional bend in the fault.

Notes on Deformation modeling

Elastic modeling of fault slip to compare with the observed deformation was performed using the Stanford Poly3D boundary element program (Thomas, 1993). This program calculates the surface deformation caused by dislocations on polygons (we used triangles or rectangles depending on the complexity of the fault geometry) embedded in a homogeneous elastic half space. We divided the fault surfaces into regular grids of patches and calculated the Green's functions that relate unit slip on each patch to the line-of-sight displacement for each sample of the resampled InSAR data. We used a constant line-of-sight approximation for each track because the 38 x 41 km area of the time series analysis has little variation in the line-of-sight vector (about 2°).

We investigated a number of fault models for the the afterslip component of the postseismic deformation. The simplest model was a single planar rectangle in the location of the main rupture of the preferred coseismic solution of Funning et al. (Funning et al., 2005), with a dip of 85.5° E. This fault was divided up into 25 patches along strike by 10 patches down dip to a depth of 10 km (1 by 1 km patches), with the rake constrained to pure right-lateral slip for the model in Fig. S8a. For the joint model with the shallow fault contraction (Fig. 4), the main fault used in afterslip modeling had a near-vertical dip and the same number of patches (25 by 10), but in a smaller fault area of 16 km along strike

and 7 km down dip so the patch size was about 0.6 km by 0.7 km. Again for the joint model, the rake was constrained to strike-slip.

Another fault afterslip model used the two faults of the preferred coseismic solution of Funning et al. (Funning et al., 2005), with the rakes of the two faults fixed to the same values as in the coseismic solution. The optimal afterslip using this fault model is shown in Fig. S7, and the residuals are shown in Fig. S8b.

The elastic models of the fault zone contraction were arranged in a way similar to the fault models with a regular grid of Mogi volume change sources instead of fault dislocation patches. The shallow fault zone was divided into six segments with varying strikes to follow the bends in the subsidence zone. Each segment was approximated as a near-vertical rectangle (dipping 89° west) down to a depth of 1 km, and then subdivided into a regular grid with a spacing of 100 m in depth and approximately 250 m along strike. Mogi volume change sources (Masterlark, 2007; Mossop and Segall, 1997) were placed at the centers of the grid rectangles, with a total of 32 columns of sources along the length of the fault zone and 10 rows in depth. The Mogi volume change in a homogeneous elastic half space equations (Masterlark, 2007) were used to calculate the Green's functions relating surface deformation to unit volume change of each source. The homogeneous assumption of the Mogi source model can affect the apparent depth of the deformation sources (Masterlark, 2007). The only independent information on the elastic structure of the Bam fault zone and surrounding rocks is the seismic velocity tomography of Sadeghi et al. (Sadeghi et al., 2006) which has only a coarse resolution of roughly 5 km horizontally and 3 km vertically, so a more complex model of the shallow elastic structure would be completely unconstrained.

Notes on Source strength inversions

A Laplacian smoothing function constraint was added to the Green's functions to reduce unrealistic fluctuations between adjacent fault slip patches or Mogi sources in the optimization process. We used a non-negative least squares inversion with a tunable smoothing factor (Jonsson et al., 2002) to determine the optimum distribution of Mogi source volume changes or fault patch slip magnitudes that minimizes the misfit to the data samples and the smoothing function. The rake of fault slip was held constant.

By adding more degrees of freedom we fit the data better. As the smoothing factor (κ) goes to zero the solution becomes more heterogeneous and the fit better. Starting from large values (i.e. κ=100, since the data are in meters, but the fault patch dimensions in kilometers) and progressing to smaller values, there is an initial rapid reduction in model to data misfit. As κ is reduced there is a corner in the misfit versus κ, beyond which lowering κ increases slip heterogeneity without significantly lowering the misfit. For these data and joint fault slip and Mogi contraction model, this value was around 100 for the fault slip and 0.01 for the Mogi sources, and the resulting synthetic LOS displacements and slip model are shown in Figs. 4a-b, and Fig. 4c, respectively.

Notes on Poroelastic rebound modeling

Poroelastic rebound has been observed using InSAR on large scales where strike-slip earthquakes have compressed or expanded the rocks through a large volume of the crust in Iceland (Jónsson et al., 2003) and California (Peltzer et al., 1998). We implemented a first-order method for calculating this effect by performing a slip inversion for the coseismic slip using the preferred two-fault model (Funning et al., 2005), but with an elastic half space with an "undrained" Poisson's ratio (0.28). Then we took the optimal slip distribution and ran forward model calculations of the surface

displacements with the undrained and drained (0.25) Poisson's ratios. The difference between the undrained and drained displacement fields is an approximation of the expected postseismic deformation due to relaxation of the coseismic pore-pressure changes, assuming a homogeneous elastic and porosity structure (Peltzer et al., 1998). Our calculation for the predicted poroelastic rebound after the Bam earthquake are shown in Fig. S9.

Supporting Figures

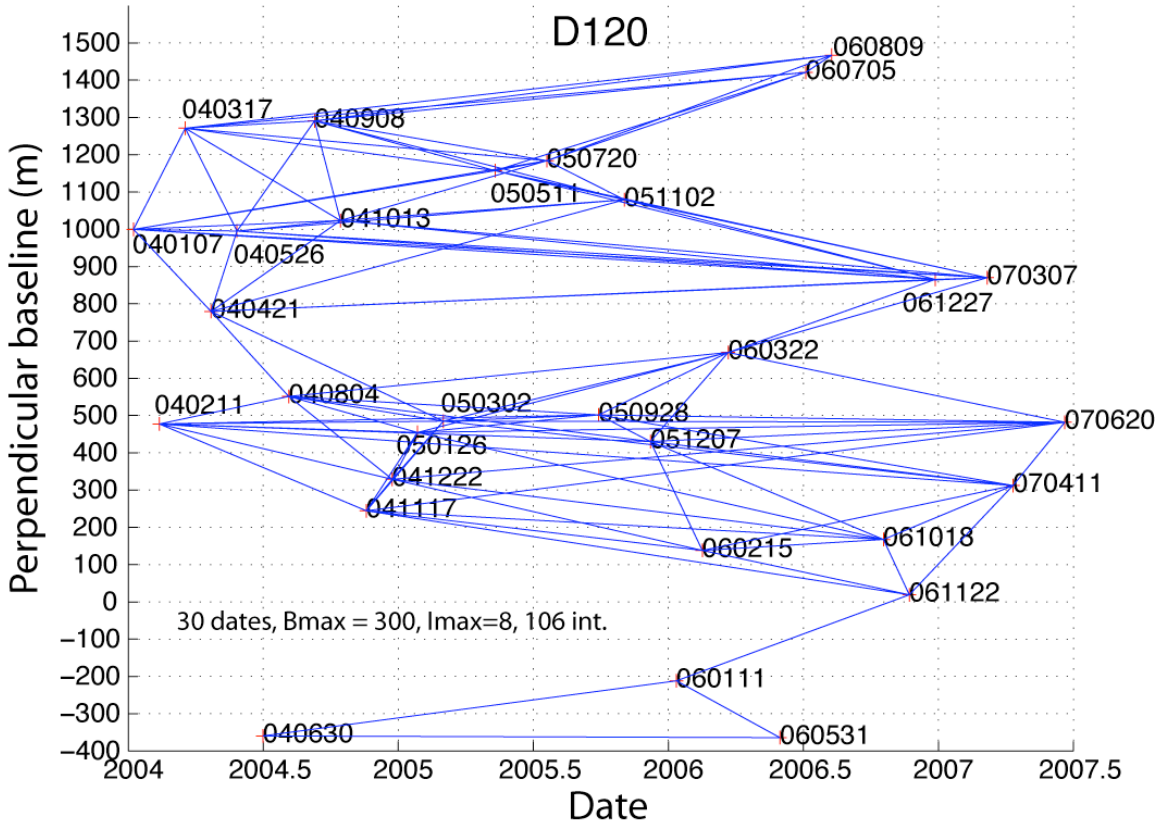

Figure S1: Plot of 106 interferogram pairs used for descending track 120

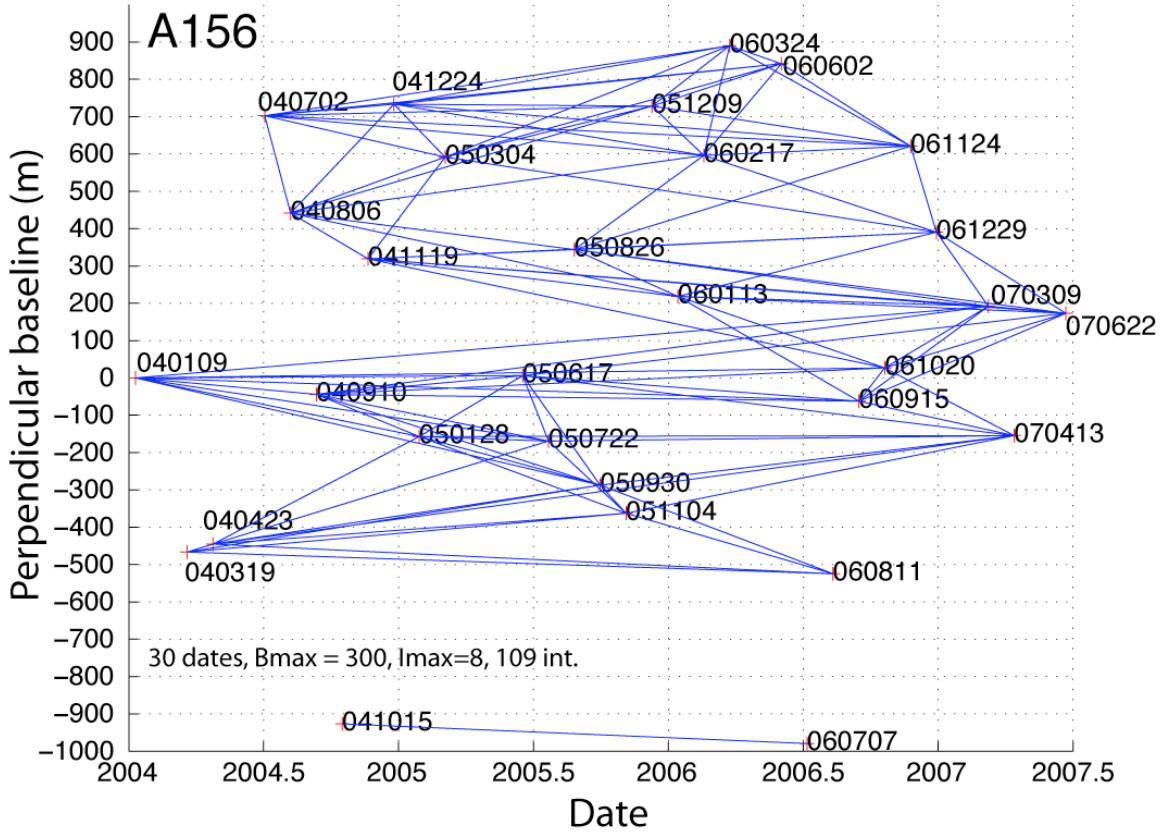

Figure S2: Plot of 109 interferogram pairs used for ascending track 156

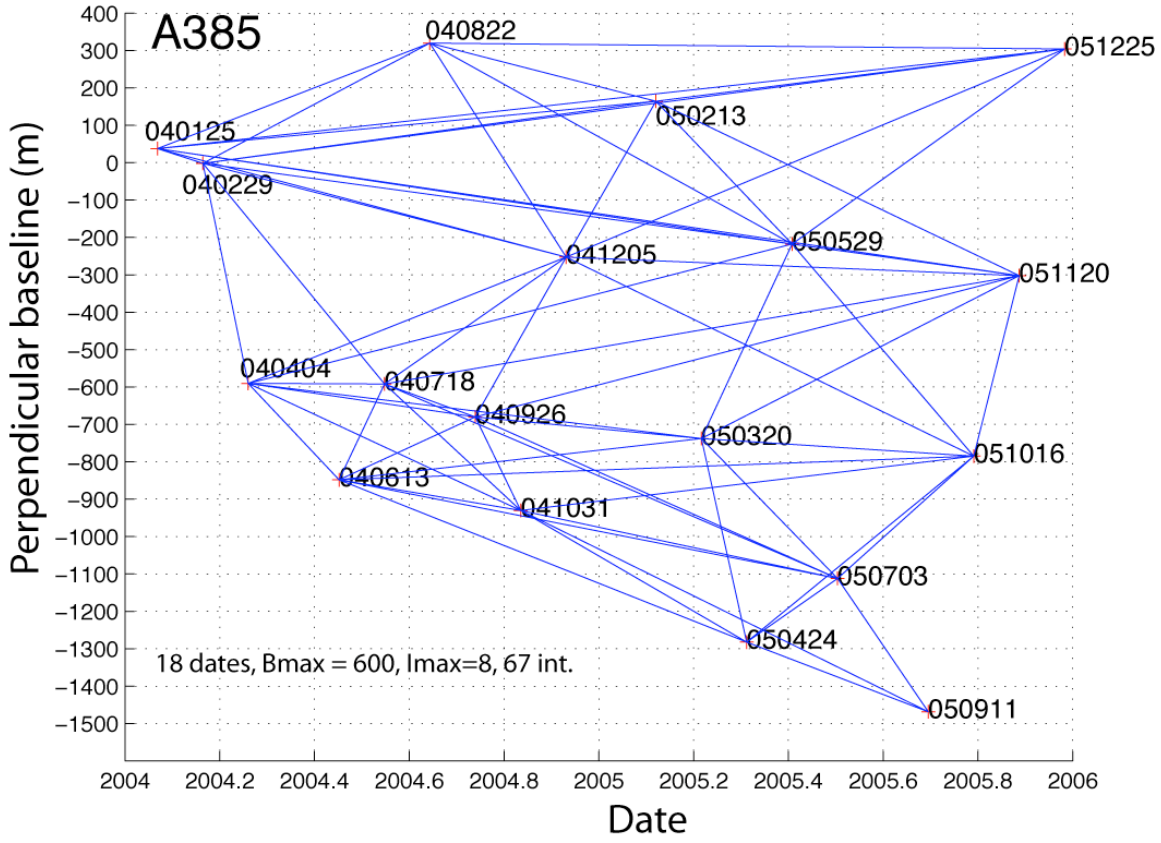

Figure S3: Plot of 67 interferogram pairs used for ascending track 385

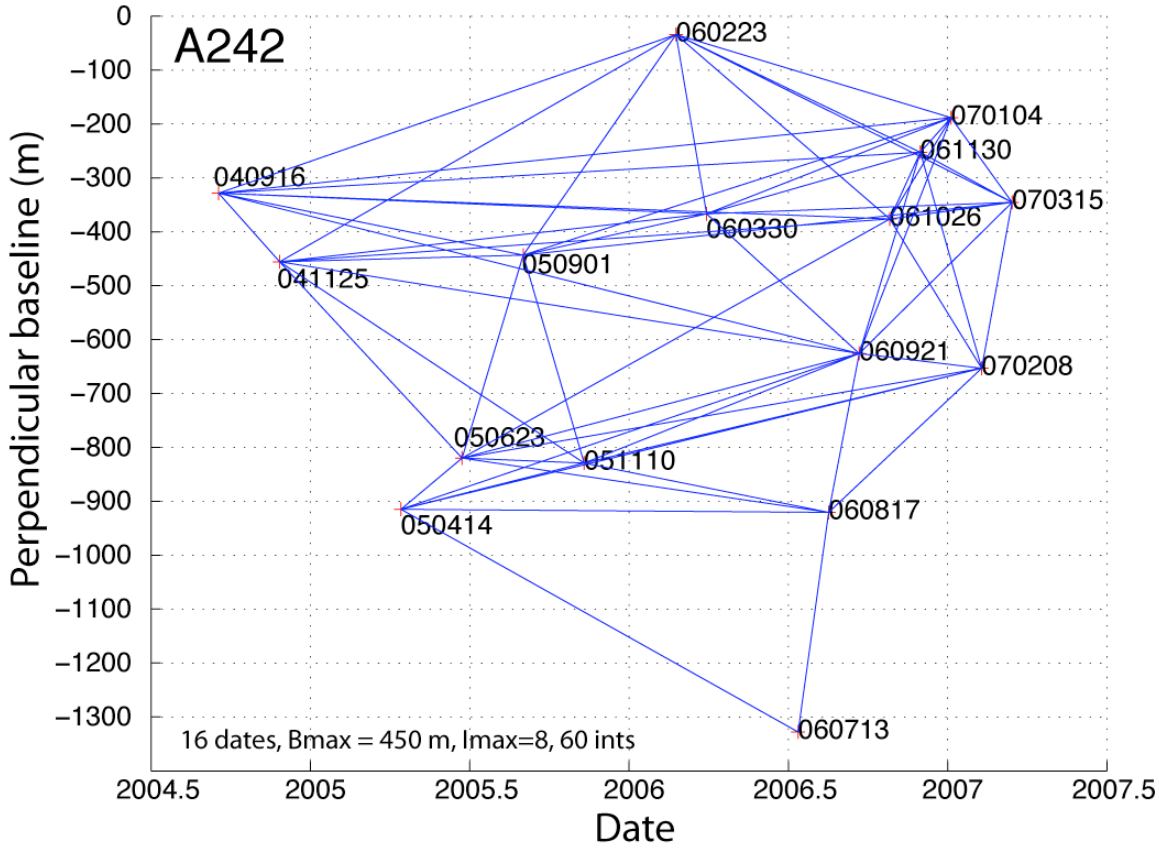

Figure S4: Plot of 60 interferogram pairs used for ascending track 242

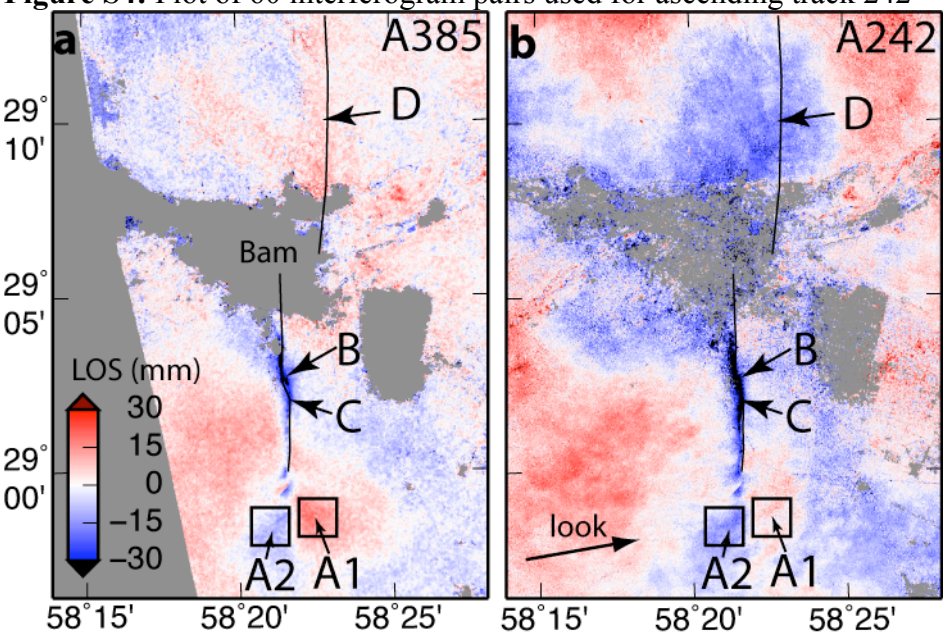

Figure S5. Estimated total postseismic deformation for ascending tracks 385 and 242.

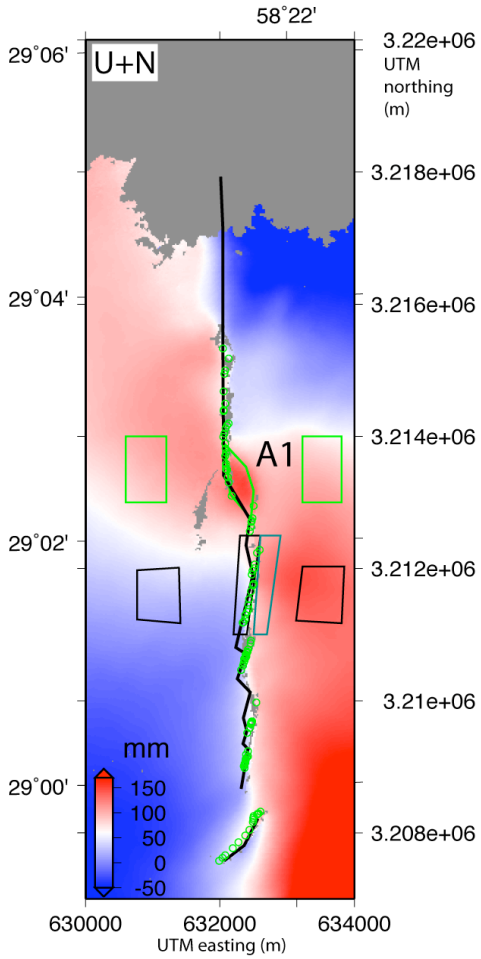

Figure S6. Coseismic up - north component of deformation in mm for same area as Fig. 3.

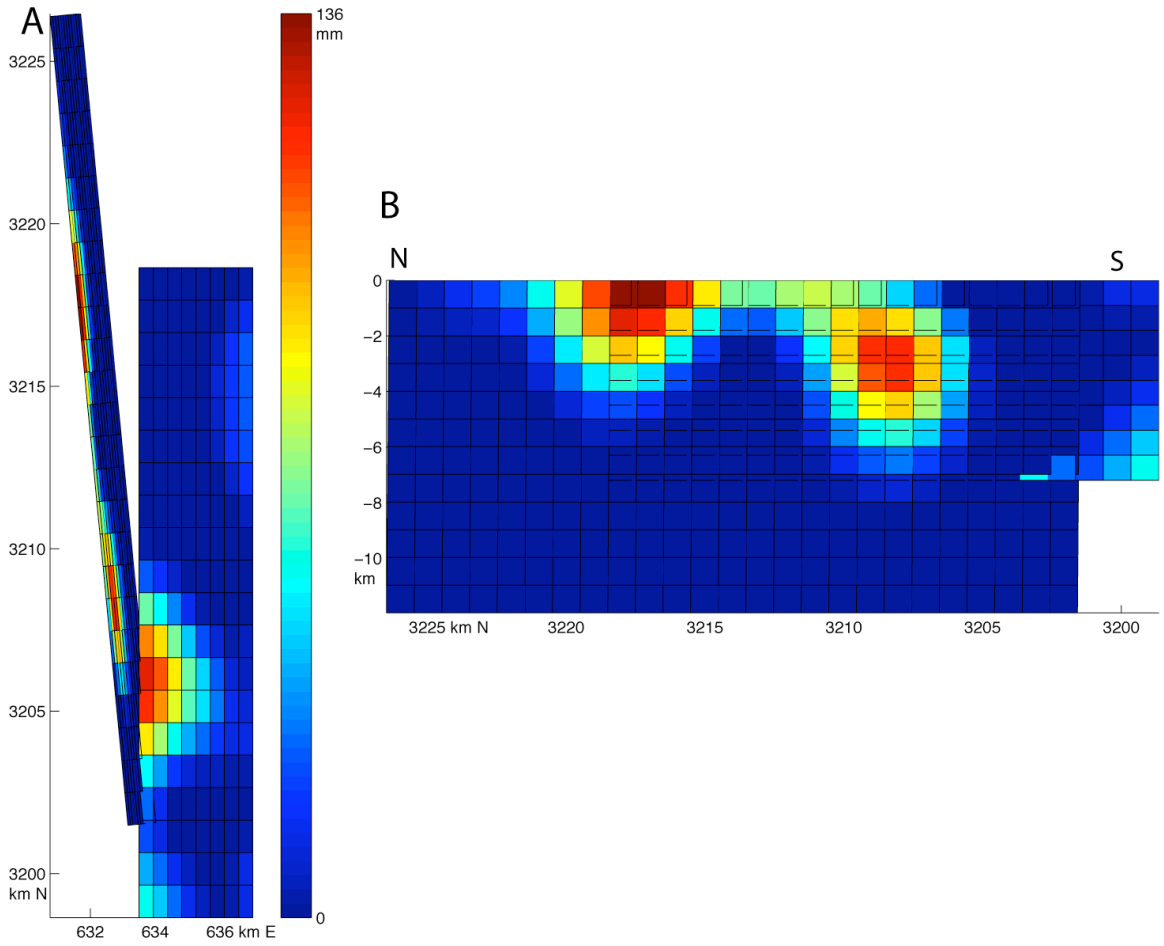

Figure S7. Postseismic afterslip model using fault parameters of (Funning et al., 2005). (A) vertical or map view of faults, with the moderately west-dipping secondary fault most prominent. (B) view from the west, showing slip on the near-vertical main fault.

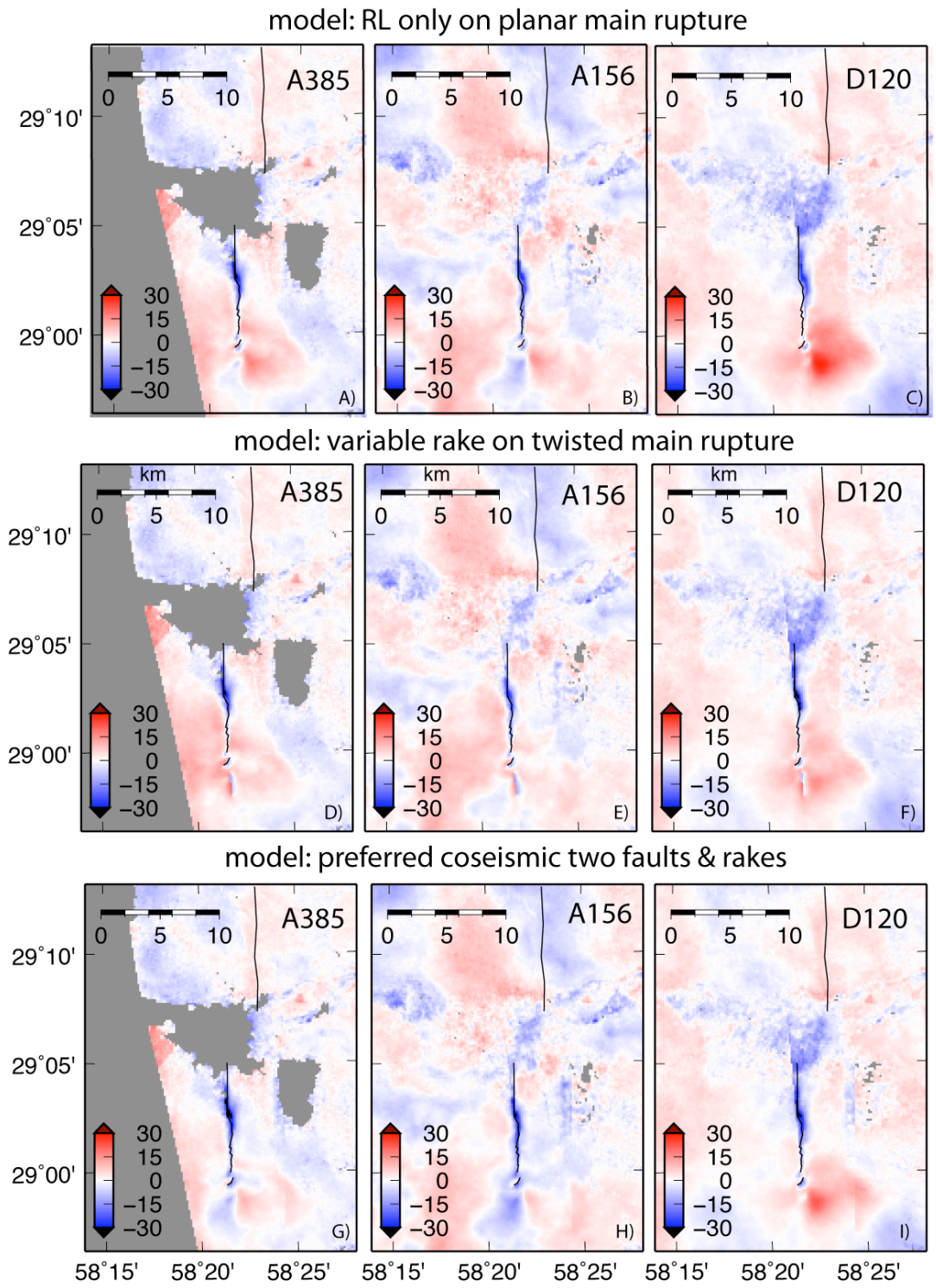

Figure S8. Comparison of residuals for three different distributed afterslip models subtracted from the estimated total deformation data for tracks A385, A156 and D120. A-C) Strike slip only on main fault. D-F) Variable rake on a twisted fault following main rupture in north and central parts and then turning to shallower east dip to south. G-I) Two fault model with same faults and slip directions as coseismic model of (Funning et al., 2005). Slip distribution shown in Figure S7.

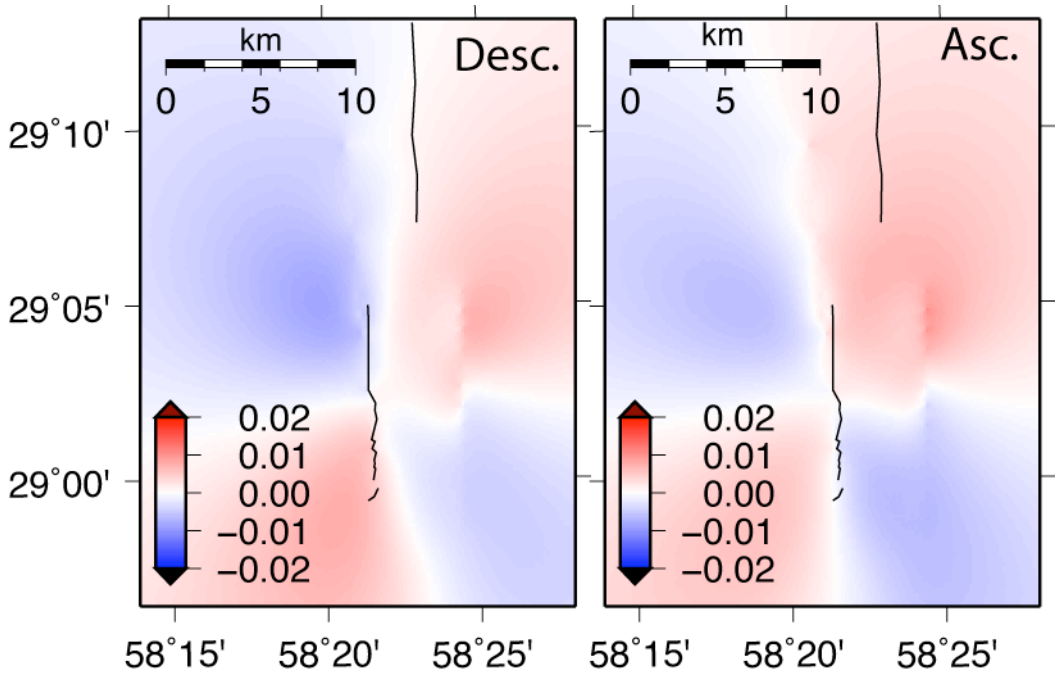

Figure S9. Predicted poroelastic surface deformation in meters computed from coseismic slip distribution (Funning et al., 2005) taking difference between forward models with Poisson's ratios 0.28 and 0.25.

Supporting Tables

Table S1: List of 30 Envisat descending track 120 SAR scenes used in time series analysis

Decimal year	Perp. Baseline (m)	Orbit	Date
2004.01916495551	999.522643446199	9693	20040107
2004.11498973306	477.318087392326	10194	20040211*
2004.21081451061	1270.93135703757	10695	20040317
2004.30663928816	779.257858700535	11196	20040421
2004.40246406571	995.134220863505	11697	20040526
2004.49828884326	-359.825019859789	12198	20040630
2004.59411362081	551.176324099638	12699	20040804
2004.68993839836	1290.5617359582	13200	20040908
2004.78576317591	1023.24880516476	13701	20041013
2004.88158795346	244.545555388001	14202	20041117
2004.97741273101	328.918638850461	14703	20041222
2005.07118412047	454.714860243467	15204	20050126
2005.16700889801	485.182574309287	15705	20050302
2005.35865845311	1156.98901598081	16707	20050511
2005.55030800821	1183.80253911802	17709	20050720
2005.74195756331	501.653204406496	18711	20050928
2005.83778234086	1079.22911134049	19212	20051102
2005.93360711841	430.254389947372	19713	20051207
2006.03011635866	-211.762732706218	20214	20060111

2006.12594113621	137.963411050893	20715	20060215
2006.22176591376	669.519142827148	21216	20060322
2006.41341546886	-364.119949699757	22218	20060531
2006.50924024641	1420.84360395461	22719	20060705
2006.60506502396	1467.04829556412	23220	20060809
2006.79671457906	167.721182583832	24222	20061018
2006.89253935661	19.1490258783452	24723	20061122
2006.98836413415	865.167773290005	25224	20061227
2007.18069815195	869.835931368755	26226	20070307
2007.2765229295	312.47304320021	26727	20070411
2007.4681724846	482.020133894113	27729	20070620

* reference scene used in time series analysis

Table S2: List of 30 Envisat ascending track 156 SAR scenes used in time series analysis

Decimal year	Perp. Baseline (m)	Orbit	Date (YearMonthDay)
2004.02464065708	0	9729	20040109
2004.21629021218	-466.43986885618	10731	20040319
2004.31211498973	-445.14162169418	11232	20040423
2004.50376454483	702.672394259665	12234	20040702
2004.59958932238	441.514178766409	12735	20040806
2004.69541409993	-44.2072085552741	13236	20040910*
2004.79123887748	-926.727084850696	13737	20041015
2004.88706365503	319.104818854147	14238	20041119
2004.98288843258	733.381917317329	14739	20041224
2005.07665982204	-156.945286169732	15240	20050128
2005.17248459959	591.593471702803	15741	20050304
2005.45995893224	6.06852813800762	17244	20050617
2005.55578370979	-168.935201755142	17745	20050722
2005.65160848734	343.910468300378	18246	20050826
2005.74743326489	-286.944558361881	18747	20050930
2005.84325804244	-362.764482986862	19248	20051104
2005.93908281999	728.109579096175	19749	20051209
2006.03559206023	218.055308235023	20250	20060113
2006.13141683778	596.075279297627	20751	20060217
2006.22724161533	889.649270624319	21252	20060324
2006.41889117043	841.510654839569	22254	20060602
2006.51471594798	-979.52194550921	22755	20060707
2006.61054072553	-524.78508180993	23256	20060811
2006.70636550308	-62.1518523964806	23757	20060915

* reference scene used in time series analysis

Table S3: List of 18 Envisat ascending track 385 SAR scenes used in time series analysis

Decimal year	Perp. Baseline	Orbit	Date
2004.06844626968	37.6636709349892	9958	20040125
2004.16427104723	-2.12097730917725	10459	20040229*
2004.26009582478	-590.578391294664	10960	20040404
2004.45174537988	-848.366020084915	11962	20040613

2004.54757015743	-591.858916396424	12463	20040718
2004.64339493498	319.655586710036	12964	20040822
2004.73921971253	-680.195411959407	13465	20040926
2004.83504449008	-930.246860737561	13966	20041031
2004.93086926762	-252.572438713887	14467	20041205
2005.12046543463	164.1977489084	15469	20050213
2005.21629021218	-737.95708472339	15970	20050320
2005.31211498973	-1282.16621179795	16471	20050424
2005.40793976728	-217.437704729905	16972	20050529
2005.50376454483	-1112.06071621994	17473	20050703
2005.69541409993	-1468.48669951829	18475	20050911
2005.79123887748	-784.765553698839	18976	20051016
2005.88706365503	-302.346030682328	19477	20051120
2005.98288843258	303.833150508706	19978	20051225

* reference scene used in time series analysis

Table S4: List of 16 Envisat ascending track 242 SAR scenes used in time series analysis

Decimal year	Perp. Baseline	Orbit	Date
2004.71184120465	-328.602897621352	13322	20040916*
2004.90349075975	-455.674462815809	14324	20041125
2005.28473648186	-914.676454728105	16328	20050414
2005.47638603696	-819.96701708357	17330	20050623
2005.66803559206	-443.203326426056	18332	20050901
2005.85968514716	-829.131077241684	19334	20051110
2006.14784394251	-34.0554526695719	20837	20060223
2006.24366872005	-366.928156284815	21338	20060330
2006.5311430527	-1327.75758671496	22841	20060713
2006.62696783025	-920.372967919278	23342	20060817
2006.7227926078	-625.971435512159	23843	20060921
2006.81861738535	-376.296090652891	24344	20061026
2006.9144421629	-252.497201764719	24845	20061130
2007.01095140315	-188.275371203803	25346	20070104
2007.1067761807	-653.136625861673	25847	20070208
2007.20260095825	-345.394529458229	26348	20070315

* reference scene used in time series analysis

Table S5: Line-of-sight vectors for InSAR scenes at Bam.

Track	East	North	Up
D120	0.39	-0.093	0.91
A156	-0.39	-0.093	0.91
A385	-0.33	-0.076	0.94
A242	-0.64	-0.149	0.75

Supporting References

Berardino, P., Fornaro, G., Lanari, R., and Sansosti, E., 2002, A new algorithm for surface deformation monitoring based on small baseline differential SAR interferograms: IEEE Trans. Geosci. Remote Sens., v. 40, p. 2375-2383.

Chen, C.W., and Zebker, H.A., 2002, Phase unwrapping for large SAR interferograms: statistical segmentation and generalized network models: Geoscience and Remote Sensing, IEEE Transactions on,, v. 40, p. 1709-1719.

Fielding, E.J., Talebian, M., Rosen, P.A., Nazari, H., Jackson, J.A., Ghorashi, M., and Walker, R., 2005, Surface ruptures and building damage of the 2003 Bam, Iran, earthquake mapped by satellite synthetic aperture radar interferometric correlation: J. Geophys. Res., v. 110, p. B03302, doi:10.1029/2004JB003299.

Funning, G.J., Parsons, B.E., Wright, T.J., Jackson, J.A., and Fielding, E.J., 2005, Surface displacements and source parameters of the 2003 Bam (Iran) earthquake from Envisat advanced synthetic aperture radar imagery: J. Geophys. Res., v. 110, p. B09406,doi:10.1029/2004JB003338.

Jónsson, S., Segall, P., Pedersen, R., and Bjornsson, G., 2003, Post-earthquake ground movements correlated to pore-pressure transients: Nature, v. 424, p. 179-83.

Jónsson, S., Zebker, H., Segall, P., and Amelung, F., 2002, Fault slip distribution of the 1999 Mw 7.1 Hector Mine, California, earthquake, estimated from satellite radar and GPS measurements: Bulletin of the Seismological Society of America, v. 92, p. 1377-1389.

Masterlark, T., 2007, Magma intrusion and deformation predictions: Sensitivities to the Mogi assumptions: Journal of Geophysical Research, v. 112, p. B06419, doi:10.1029/2006JB004860.

Mossop, A., and Segall, P., 1997, Subsidence at The Geysers geothermal field, N. California from a comparison of GPS and leveling surveys: Geophysical Research Letters, v. 24, p. 1839–1842.

Peltzer, G., Rosen, P., Rogez, F., and Hudnut, K., 1998, Poroelastic rebound along the Landers 1992 earthquake surface rupture: J. Geophys. Res., v. 103, p. 30131-30145.

Rosen, P.A., Hensley, S., Peltzer, G., and Simons, M., 2004, Updated repeat orbit interferometry package released: Eos, Transactions, American Geophysical Union, v. 85, p. 47.

Sadeghi, H., Aghda, S.M.F., Suzuki, S., and Nakamura, T., 2006, 3-D velocity structure of the 2003 Bam earthquake area (SE Iran): Existence of a low-Poisson's ratio layer and its relation to heavy damage: Tectonophysics, v. 417, p. 269-283.

Savage, J.C., Svarc, J.L., and Yu, S.B., 2005, Postseismic relaxation and transient creep: J. Geophys. Res, v. 110, p. doi:10.1029/2005JB003687, B11402.

Thomas, A.L., 1993, Poly3D: a three-dimensional, polygonal element, displacement discontinuity boundary element computer program with applications to fractures, faults, and cavities in the Earth's crust [M.Sc. thesis]: Stanford, California, USA, Stanford University.